

Robustness of Neural Networks for CMB Polarization Foreground Removal

Luca Gomez Bachar^{1, *}, Cora Dvorkin², and Alberto Daniel Supanitsky¹

¹*Instituto de Tecnologías en Detección y Astropartículas (CNEA, CONICET, UNSAM), Centro Atómico Constituyentes, San Martín, Buenos Aires CP B1650KNA, Argentina*

²*Department of Physics, Harvard University, Cambridge, MA 02138, USA*
(Dated: March 16, 2026)

The detection of Cosmic Microwave Background primordial B -mode polarization would constitute a “smoking gun” signal of primordial gravitational waves. However, this measurement requires accurate removal of polarized Galactic foregrounds to avoid systematic biases when estimating the tensor-to-scalar ratio. Methods based on Machine Learning techniques (ML), such as Convolutional Neural Networks (CNNs), have recently been proposed as alternative foreground cleaning techniques, but their applicability to real data relies on their ability to generalize beyond the models assumed during training. In this work, we focus on a variety of foreground models (FMs) used for training and conduct a systematic study of the generalization properties of a CNN-based method. We train various CNN architectures on simulations generated from different Galactic FMs, and test their performance on models not used during the training. By characterizing the statistical properties of the FMs using variance, skewness, and Shannon entropy, we define a statistical complexity hierarchy among them. We show that training on the more complex FMs reduces bias and improves precision when testing on unseen FMs, whereas training on the simplest model could introduce systematic errors. These results evidence that a lack of generalization is a relevant source of systematic uncertainty, and emphasize the importance of understanding the impact of the models assumed during training in ML-based methods before applying them to real data.

I. INTRODUCTION

The standard cosmological model (Λ CDM) provides a successful description of the evolution of the universe. Nevertheless, several fundamental questions remain open, some of them regarding the physics of the very early Universe. Inflationary scenarios were originally introduced to explain conceptual challenges such as the horizon and flatness problems and, more generally, to provide a mechanism for generating primordial perturbations [1, 2]. A generic prediction of inflation is the existence of a stochastic background of primordial gravitational waves (PGW), whose detection would provide the first observational window into physics at energy scales far beyond the reach of terrestrial experiments.

Tensor perturbations of the metric give rise to a non-vanishing PGW power spectrum. These tensor modes leave a distinctive imprint on the polarization of the Cosmic Microwave Background (CMB), sourcing both E - and B -mode polarization, while scalar perturbations under linear evolution generate only E -modes. As a consequence, a primordial B -mode signal constitutes a direct probe of inflationary physics and is commonly parametrized by the tensor-to-scalar ratio r . A detection of $r > 0$ would therefore represent a smoking gun for the inflationary epoch. Currently, the best constraint is obtained from the measurements by the BICEP/Keck Collaboration [3] reaching $r < 0.032$, when combined with the Planck Release 4 (PR4) and Baryon Acoustic Oscillations [4].

Measuring the primordial B -mode signal is challenging. In addition to instrumental noise [5] and systematic effects associated with the optical design of CMB experiments [6, 7], weak gravitational lensing converts E -modes into B -modes [8], producing a secondary signal that must be mitigated through delensing techniques [9]. Furthermore, polarized Galactic foregrounds, which are dominated primarily by synchrotron radiation and thermal dust emission, among other polarized sources, contaminate the observed CMB maps and can mimic the primordial B -mode signal [10–13]. An inaccurate treatment of these foregrounds can lead to biased estimates of r , making foreground removal a dominant source of systematic uncertainty in current and future CMB polarization experiments [14].

Several foreground-cleaning techniques have been developed to address this problem. Parametric approaches rely on explicit modeling of the frequency dependence of foreground components [15–17], while blind methods derived from the Internal Linear Combination (ILC) aim to minimize foreground contamination without strong assumptions of the Foreground Model (FM) [18–24]. Although traditional methods have achieved considerable success, their performance could be insufficient to reach the sensitivity required for detecting primordial B -modes in forthcoming experiments [14], motivating the exploration of alternative approaches.

In recent years, machine learning (ML) techniques have been applied to several fields in cosmology and astrophysics [25–30]. In particular, several ML-based approaches have been proposed as tools for CMB component separation, such as Convolutional Neural Networks (CNNs) techniques [31–34], Diffusion Models (DMs) [35],

* luca.gomez@iteda.gob.ar

and other approaches which are not based on image processing, like ML-based ILC extensions [36–38].

In this work, we study the generalization properties of a CNN-based foreground-cleaning method applied to CMB polarization, adopting as a case study a CMB-S4-like small aperture telescope (SAT) [39, 40]. Rather than assuming that neural networks automatically generalize across different FMs, we explicitly test this assumption by training CNNs on simulations generated from specific template-based Galactic FMs and evaluating their performance on other models not seen during the training. To this end, we introduce performance metrics to quantify both the accuracy and precision of the reconstructed CMB signal and to identify potential biases and uncertainty arising from the lack of generalization.

To interpret these results, we quantify statistical properties (variance, skewness, and Shannon entropy) of the FMs considered in this work. We show that these statistics serve as a measure of foreground complexity. In this sense, generalization emerges not merely as a machine learning concern but as a physically relevant property for controlling the systematic uncertainty in the estimation of cosmological parameters.

This paper is organized as follows. In Section II we describe the simulation pipeline used to generate CMB polarization maps, instrumental noise, and Galactic foregrounds. In Section III we present the foreground-cleaning methods considered in this work, including the traditional techniques and the CNN-based approach. In Section IV we introduce our generalization hypothesis, compute the statistical properties of the FMs, and define the performance metrics used in the analysis. Finally, in Section V we present and discuss our results.

II. SIMULATIONS

The goal of this paper is to analyze the impact of the simulation-based technique on the performance of the CNN-based method. To this end, we define a procedure to generate simulations to train and test the networks, including different FMs. We provide the code used here¹. Our simulations include three components: lensed CMB polarization maps, instrumental noise realization maps, and polarized Galactic foregrounds. To generate our simulations, we use the Python library Healpy² [41, 42], and for all calculations in this paper we adopt $N_{\text{side}} = 256$, leading to a $\ell_{\text{max}} \approx 767$, which is enough to target the recombination bump at $\ell \approx 100$. We perform the simulations using the spin-two polarization Stokes Parameters Q and U , which are physical quantities that can be measured directly by a telescope.

As our analysis focuses on ground-based experiments, we use a partial-sky approach. To account for that, we

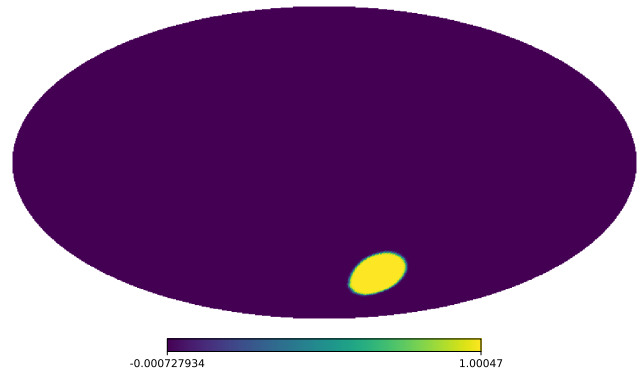


FIG. 1. Apodized version of the mask applied to the full-sky simulations. The observed patch is centered at (RA, DEC) = $(316^\circ, -56^\circ)$, corresponding to the center of the sky patch observed by the QUBIC instrument. The apodization scale applied in this mask is 0.5° .

adopt a mask centered at the coordinates (RA, DEC) = $(316^\circ, -56^\circ)$, corresponding to the center of the sky patch observed by the QUBIC instrument [43–45]. We use an angular aperture with a radius of 14° centered on this point. To compute the angular spectra, we adopt an apodized version of this mask, which is shown in Fig. 1, with an apodization scale of 0.5° . The sky patch studied in this work corresponds to a sky fraction of $f_{\text{sky}} \approx 0.015$.

For the CNN-based method, we generate simulated training, validation, and testing sets with 1000, 300 and 300 polarization maps, respectively. For each simulation, we generate the lensed CMB, the instrumental noise, and the Galactic foregrounds. In the rest of this section, we detail the process for generating the components mentioned above.

A. Lensed CMB polarization maps

To generate lensed realizations of CMB polarization maps, we start by computing the primordial power spectra using CAMB³ [46] assuming a fixed cosmology. We adopt the Planck 2018 best-fit cosmological parameters [47], fixing $r = 0$ for all the simulations in this work. These primordial power spectra are then used to generate lensed realizations of the Q and U CMB polarization maps with Lenspyx⁴ [48]. Since we work in units of μK_{CMB} , we use the same lensed CMB polarization maps for all frequency channels. We compute the pseudo- C_ℓ s of the lensed CMB polarization maps using the Python library Namaster⁵ [49]. To perform this computation, we apply the mask shown in Fig 1 to the Q and U maps. We then use

¹ <https://github.com/LucaGomez/cNNbP>

² <https://github.com/healpy/healpy>

³ <https://github.com/cmbant/CAMB>

⁴ <https://github.com/carronj/lenspyx>

⁵ <https://github.com/LSSTDESC/NaMaster/>

Namaster to estimate the pseudo- C_ℓ , including B -mode purification [50], and adopting a binning scheme of 12 multipoles per bin. The pseudo- C_ℓ s computed following this procedure are used as the ground-truth, C_ℓ^{True} , to measure the performance of the methods in the analysis of the results.

B. Instrumental noise

To simulate instrumental noise, it is necessary to use a telescope model. Since our goal is to target primordial B -modes at $\ell \approx 100$, corresponding to the recombination bump, we adopt a SAT model. Several collaborations use SATs to measure large angular scales, targeting the recombination bump of the B -mode of polarization. Some current examples are the Simons Observatory [51] and BICEP [52, 53], and future ones are QUBIC [43–45] and CMB-S4 [40]. In this paper, we adopt the CMB-S4 SAT model for simplicity. The CMB-S4 SAT measures each frequency band with independent detectors [40], allowing us to safely assume an uncorrelated noise model across frequency bands.

We therefore generate Gaussian noise realizations for all the frequency bands considered, assuming a $1/f$ -type noise power spectrum:

$$N_\ell^{X,\nu} = \Delta^\nu \left(1 + \left(\frac{\ell}{\ell_{\text{knee}}^\nu} \right)^{\alpha_{\text{knee}}^\nu} \right), \quad (1)$$

where $X = \{E, B\}$, and the parameters of the noise power spectrum can differ between frequency bands [9, 14, 33]. The parameters assumed for the SAT telescope are listed in Table I [9]. To generate Gaussian noise realizations, we use the Synfast function from Healpy. This approach transforms the full-sky E - and B -mode realizations generated with the spectrum from Eq. 1 into full-sky Q and U maps. After this transformation, we apply the mask to get the partial-sky noise realization. This noise model corresponds to four years of observations taken by the adopted SAT model [17].

SAT	Band	Beam	Spectra parameters		
	(GHz)	(arcmin)	Δ^ν	ℓ_{knee}^ν	α_{knee}^ν
	30	72.8	3.74	60	-2.2
	40	72.8	4.73	60	-2.2
	85	25.5	0.93	60	-2.2
	95	22.7	0.82	60	-2.2
	145	25.5	1.25	65	-3.1
	155	22.7	1.34	65	-3.1
	220	13.0	3.48	65	-3.1
	270	13.0	8.08	65	-3.1

TABLE I. Small aperture telescope model assumed for the simulations.

C. Foreground models

The foreground models studied in this work are based on templates derived from observations. We consider three models for training the CNNs. The first one is a model based on Gaussian fluctuations of the spectral energy distribution (SED) parameters, which we call ‘‘GP’’; the second model consists on rotating the sky before extracting the sky patch, and we call it ‘‘RP’’; and the third one is the PySM3⁶ model d11s6 [54]. The three FMs are based on templates derived from observations, which are available in PySM3 and generate full-sky realizations across all frequency bands. Our Galactic FMs include only dust and synchrotron emission, which is sufficient for the aims of this paper; additional polarized sources can be included using a similar procedure. For the FMs, we assume the same SED [55]: a modified blackbody (MBB) spectrum for dust:

$$Q_\nu^d(\hat{n}) = A_{Q,\nu_0}^d(\hat{n}) \left(\frac{\nu}{\nu_0} \right)^{\beta_d(\hat{n})} B_\nu(T_d(\hat{n})), \quad (2)$$

$$U_\nu^d(\hat{n}) = A_{U,\nu_0}^d(\hat{n}) \left(\frac{\nu}{\nu_0} \right)^{\beta_d(\hat{n})} B_\nu(T_d(\hat{n})),$$

where $B_\nu(T_d(\hat{n}))$ is the typical black body energy density at frequency ν for a temperature T_d at the direction in the sky described by \hat{n} . A_{Q,ν_0}^d and A_{U,ν_0}^d are the amplitudes, β_d is the spectral index, and $\nu_0 = 353$ GHz is the pivot frequency for polarization. For the synchrotron emission, we consider a power law dependence:

$$Q_\nu^s(\hat{n}) = A_{Q,\nu_0}^s(\hat{n}) \left(\frac{\nu}{\nu_0} \right)^{\beta_s(\hat{n})}, \quad (3)$$

$$U_\nu^s(\hat{n}) = A_{U,\nu_0}^s(\hat{n}) \left(\frac{\nu}{\nu_0} \right)^{\beta_s(\hat{n})}.$$

In addition to the three models presented above, we use two additional models implemented in PySM3, d4s2 and d12s7, only for testing the CNNs. In the following sections, we describe the details about each FM studied in this work.

1. Gaussian fluctuations in the SED parameters (GP)

This model is based on the PySM3 model d1s1. For the dust contribution (d1), the parameters are based on Planck 2015 observations at 353 GHz for polarization [55]. These observations are scaled to different frequencies assuming an MBB SED and using the spatially varying

⁶ <https://github.com/galsci/PySM>

temperature and spectral index obtained from the Planck data using the Commander code [55]. For the synchrotron (s1), the templates are based on WMAP 9-year 23 GHz Q/U maps [56] and are scaled to different frequencies using a power-law assumption. To generate variations in the fixed d1s1 template, we introduce fluctuations in the parameters appearing in Eqs. 2 and 3, which affect the frequency scaling of the original template. These variations are introduced following the technique described in [33, 34]. This procedure introduces 5% variations in β_d and β_s , 10% variations for the amplitudes, and 5% variations for the dust temperature in each realization.

2. Rotating the sky before extracting the patch (RP)

This foreground model is based on the d1s2 template. The dust contribution is the same as in the GP model, and the synchrotron spectral index steepens off the Galactic plane consistently with WMAP. Instead of introducing random variations in the parameters, as we do in GP, we rotate the full-sky map by a random angle before extracting the sky-patch shown in Fig. 1. In this approach, the pixel-to-pixel variations are larger than those obtained with the GP realizations. To avoid the inclusion of the Galactic plane in the observed patch, we set an arbitrary threshold of $40 \mu\text{K}^2$ and reject any rotation angle for which the maximum absolute value of either Q or U in the observed sky patch exceeds this threshold. This criterion is applied because the foreground intensity in these regions is orders of magnitude larger.

3. PySM3 d11s6

This foreground model corresponds to the d11s6 model of PySM3, and the variations are introduced by the library itself. For both dust and synchrotron emissions, this method introduces stochastic small-scale fluctuations generated on the fly on top of the fixed d10 and s5 templates. The d10s5 model is based on templates from the GNILC needlet-based analysis of Planck data, with reduced contamination from the cosmic infrared background and point sources compared to the Commander maps used in d1s1⁷.

4. PySM3 d4s2

This model generalizes the dust model d1 to multiple dust populations using the two-component model described in [57]. The synchrotron model s2 is the same as the one we used in RP. We include this model among the testing options for comparison with [34].

5. PySM3 d12s7

The dust contribution in this model relies on a three-dimensional model of polarized dust emission with six layers, based on [58]. The synchrotron contribution consists of a power-law with a frequency-dependent spectral index. This synchrotron model uses the same templates and spectral index map as s5, and includes a curvature term derived from the ARCADE experiment [59], along with additional small-scale random fluctuations. We include this model among the testing options, following [14].

III. FOREGROUND CLEANING METHODS

In this section, we present our procedure to remove Galactic foregrounds from CMB polarization maps. For comparison, we also perform a maximum-likelihood parametric approach and a version of the Internal Linear Combination (ILC) method applied to CMB polarization.

A. Maximum likelihood parametric method

This method assumes a frequency-dependent model for the Galactic foregrounds and the instrument. This method is implemented using the FGBuster library⁸ [15]. We use as inputs the beam-convolved, frequency-dependent contaminated and noisy maps, and the algorithm recovers the CMB, dust, and synchrotron maps. It is important to note that this method relies on estimating the parameters of a given model (e.g., Eq. 2 for dust), and therefore its performance is sensitive to the assumed frequency model. Here, we first estimate the spectral parameters and then solve a linear system of equations to obtain the amplitudes at each pixel.

B. Internal Linear Combination (ILC) method

The ILC is a blind method that does not assume a specific foreground model, although it does assume that the CMB is the same for all frequencies, which holds in μK_{CMB} units if the CMB energy density corresponds to a blackbody spectrum. In this paper, we use a pixel-domain polarization ILC adapted for polarization maps, which operates on the Q and U maps [60, 61]. In our model, we assume that

$$\hat{Q}_{\text{CMB}}(p) \pm i \hat{U}_{\text{CMB}}(p) = \sum_{j=1}^{N_\nu} \left(\omega_j^{(R)} \pm i \omega_j^{(I)} \right) \times [Q_j(p) \pm i U_j(p)], \quad (4)$$

⁷ <https://pysm3.readthedocs.io/en/latest/models.html>

⁸ <https://github.com/fgbuster/fgbuster>

where p represent the pixel in the sky, N_ν is the number of frequency bands, $Q_j(p)$ and $U_j(p)$ are the beam-convolved, frequency-dependent contaminated and noisy maps, and $\hat{Q}_{\text{CMB}}(p)$ and $\hat{U}_{\text{CMB}}(p)$ are the CMB maps estimated by the method. This technique relies on estimating the weights $\omega_j^{(R)}$ and $\omega_j^{(I)}$. The weights are obtained by minimizing the variance

$$\left\langle \left| \hat{Q}_{\text{CMB}} + i \hat{U}_{\text{CMB}} \right|^2 \right\rangle \quad (5)$$

which is the only relevant quantity under the assumption that the CMB is Gaussian [36].

Once the weights are estimated, the predicted cleaned map is obtained as the linear combination defined in Eq. 4. An important aspect of this method is that all foreground-contaminated maps must have the same angular resolution. Since it is not possible to upgrade a map's resolution, we degrade all frequency maps to the lowest resolution among the frequency bands. We find that the resolution of the 30 and 40 GHz channels is too low to obtain reliable ILC results. Therefore, to apply this method, we convolve all frequency maps to a common beam size of 25.5 arcmin and exclude the 30 and 40 GHz bands from the analysis.

C. CNN-based method

For the traditional methods described above, it is important to note that more recent and advanced techniques exist. Examples include MCMC-based estimates of spectral parameters rather than relying on the maximum-likelihood solution, as well as more complex and realistic models of the likelihood. There are also more sophisticated ILC approaches, such as the Harmonic ILC (HILC) [62], the Needlet ILC (NILC) [63], among others. The traditional methods presented in this work should therefore be understood as proof-of-concept approaches for comparison with the CNN-based method. Consequently, we do not claim that the CNN-based method outperforms state-of-the-art traditional techniques, since we are not comparing against the most recent and optimized algorithms. This is not the point of this paper.

However, both traditional methods discussed before and their upgraded versions present significant implementation challenges. The parametric approach assumes a specific FM and then estimates its parameters. As a result, any inaccuracy in the assumed model propagates directly into the reconstructed maps. The ILC method does not suffer from this limitation because it is blind to the FM, but there is a loss of information due to the fact that all input maps must be brought to a common angular resolution. Since it is not possible to increase the resolution of a map, all maps must be degraded to the resolution of the lowest-frequency channel. This process inevitably leads to a loss of small-scale information contained in the higher-resolution maps.

Motivated by these challenges, we introduce a CNN-based method that assumes a foreground model during both training and testing. During training, the CNN is expected to learn the most relevant features for removing the Galactic foregrounds. Then, the trained algorithm can be applied to data simulated from a different FM to assess its generalization capabilities and estimate the error. This method could be applied to real data if the test set contained a feasible physical model of the foregrounds and generalization was achieved, both of which depend strongly on the training set. An advantage of this approach is that it does not require degrading the angular resolution of the input maps. Instead, the CNN is fed with the Q and U frequency maps at each frequency band's original resolution, allowing it to use all the information in the input maps.

The CNN-based method consists of training a neural network that takes as input the foreground-contaminated and noisy polarization maps and produces the corresponding noisy CMB map at the target frequency, which in our case is 220 GHz. In the following sections, we describe the relevant details of the method.

1. Data pre-processing

In Section II, we describe the procedure used to generate partial-sky simulations including CMB, Galactic foregrounds, and instrumental noise. In this section, we describe how we transform the Healpy sky maps into the input of the CNN-based method. Since CNNs operate on images, the $12 \times N_{\text{side}}^2$ -dimensional Healpy sky maps must be converted into two-dimensional blocks with shape $(N_{\text{size}}, N_{\text{size}})$, where N_{size} refers to the number of pixels of the block and is not necessarily equal to N_{side} . This transformation is applied to both Q and U maps for each frequency band independently. To perform this conversion, we follow the technique described in [33]. This operation is not a projection; instead, it is a bijective mapping in which the pixels belonging to each N_{side}^2 sky patch are reorganized one-to-one into a $(N_{\text{side}}, N_{\text{side}})$ block.

Due to the limited sky area covered by the observed patch, several pixels within the corresponding sky patch (with size $(N_{\text{side}}, N_{\text{side}})$) are fixed to zero. This allows us to reorganize the pixels extracted from a sky with $N_{\text{side}} = 256$ into a block with shape $(N_{\text{size}} = 128, N_{\text{size}} = 128)$. Since CNN training is computationally expensive, reducing the input size is advantageous, as it enables larger batch sizes and reduces overall training time.

Finally, once the foreground-contaminated and noisy blocks are constructed, we compute and store the maximum absolute pixel value across all channels and normalize the input blocks by this factor. This normalization ensures that all input channels lie in the range $[-1, 1]$. Since the normalization factor is saved, the CNN output can later be rescaled to compute the angular power spectra.

2. Training of the CNNs

The training procedure of the CNN-based method begins with selecting a network architecture, followed by generating training and validation sets of 1000 and 300 foreground-contaminated blocks with added noise, respectively, as described in Section III C 1. The CNN takes inputs with shape $(N_{\text{batch}}, N_{\text{channels}}, N_{\text{size}}, N_{\text{size}})$. In this work, we use $N_{\text{batch}} = 32$ and $N_{\text{channels}} = 16$, corresponding to eight frequency bands for each of the Q and U polarization maps. As discussed in Section III C 1, the image size is $N_{\text{size}} = 128$ for simulations with $N_{\text{side}} = 256$.

The output of the CNN is a tensor with shape $(2, N_{\text{size}}, N_{\text{size}})$, corresponding to the reconstructed noisy CMB Q and U blocks. The training is performed over 75,000 iterations. At each iteration, N_{batch} foreground-contaminated blocks are randomly selected, stacked, and fed to the CNN. The network processes the input tensor, and the loss function consists of the Mean Absolute Error (MAE), computed by comparing the CNN output with the target noisy CMB Q and U blocks at the field level. In addition, we compute the Fast Fourier Transform (FFT) of both the output and target blocks, and include this information in the loss function as a physics-guided term [34]. The total loss function used during training is therefore identical to the one defined in [33] and is given by

$$\mathcal{L} = \mathcal{L}_{\text{MAE}} + \mathcal{L}_{\text{FFT}}. \quad (6)$$

Gradients are computed using PyTorch, and backpropagation is used to update the CNN’s trainable parameters. During training, we also evaluate the validation loss by applying the CNN to batches drawn from the validation set to detect overfitting.

3. CNN architectures

In this work, we consider three different CNN architectures. The first one is a UNet-type architecture (UN) with two convolutional layers per level⁹ [64]. The second architecture (UB) corresponds to the same UNet but includes batch normalization layers [65] after each convolution. The third architecture is a more complex model presented in [33], referred to here as L3¹⁰. The L3 architecture divides the input images into multiple blocks, processes each block with internal UNets, and subsequently applies convolutional layers with batch normalization and dilated convolutions to obtain the final output image. In this work, we modified the original L3 architecture to produce two output channels, corresponding to the Q and U polarization components, because the original design has only one output channel [33].

These three architectures were studied because we observed notable differences in their training behavior. In particular, the UN architecture exhibits divergences in the gradient norm during training. When batch normalization is added (UB architecture), these large gradient values disappear, indicating that batch normalization helps to control this issue. The L3 architecture, specifically designed for CMB-related applications, shows the best control over gradient behavior.

The training time for all three architectures is comparable, totaling approximately 8 hours on an A100 GPU. This is expected for the UN and UB architectures, as they have a similar number of parameters, with slight differences introduced by the additional learnable parameters in the batch normalization stages. Both architectures contain approximately 1.2×10^8 parameters, whereas the L3 architecture contains approximately 8×10^6 parameters. Despite its smaller parameter count, the L3 architecture’s increased computational complexity results in training time comparable to the other two models.

4. Testing the CNNs

After the training stage, we evaluate the performance of the CNN-based method on a test set of 300 maps generated using the same procedure described in Section III C 1. These maps are completely independent of those used during training and validation. Each testing map is processed individually: the foreground-contaminated and noisy blocks are fed through the trained CNN to obtain the predicted noisy CMB blocks. Then, we apply the inverse transformation to recover the partial-sky maps from the output blocks. After that, we compute the angular power spectra of both the target and reconstructed maps using the pseudo- C_ℓ technique implemented in NaMaster [49]. The performance of the CNN is quantified using the ratio $C_\ell^{\text{Rec},X}/C_\ell^{\text{True},X}$, where $X = E, B$.

IV. GENERALIZATION HYPOTHESIS

The goal of this work is to evaluate how training-model assumptions impact CNN performance in CMB polarization foreground cleaning. In this section, we introduce a set of statistical quantities to characterize which properties of the training data are most relevant for enabling generalization. These statistics quantify the variability and complexity of the training distribution and provide a useful framework to interpret the empirical generalization performance of the CNNs studied in this work. To simplify the discussion, we will focus on the polarization amplitude $P = \sqrt{Q^2 + U^2}$. This choice captures the overall amplitude of the polarized emission and allows for a direct comparison between different FMs.

We use a full-sky frequency-dependent FM model, and apply the 2D image mapping described in Section III C 1 to generate realizations of the polarization maps Q and U ,

⁹ <https://github.com/jaxyony/unet-pytorch/>

¹⁰ https://github.com/yanyepeng/CMBFSCNN/blob/main/cmbfscnn/CNN_models.py

with dimensions $[N_{\text{freqs}}, N_{\text{side}}, N_{\text{side}}]$. The amplitude of P at each pixel will be denoted as \mathcal{P}_{ijk}^{Mr} , where $i \in [1, N_{\text{freqs}}]$ labels the frequency channel, $j, k \in [1, N_{\text{side}}]$ label the pixel indices, M refers to the specific model assumed, and r indexes the realization number. Throughout this analysis, we consider a single-frequency channel, fixed at i , corresponding to 220 GHz.

A. Foreground models statistics

For a given FM (M), channel (i), and pixel (j, k), we define the mean over R realizations as

$$\mu[P_{ijk}^M] = \frac{1}{R} \sum_{r=1}^R P_{ijk}^{Mr}. \quad (7)$$

Using this definition, the unbiased variance is given by

$$\text{Var}[P_{ijk}^M] = \frac{1}{R-1} \sum_{r=1}^R (P_{ijk}^{Mr} - \mu[P_{ijk}^M])^2. \quad (8)$$

The mean and variance correspond to the first- and second-order moments of the distribution. For a Gaussian distribution, these quantities would fully characterize its statistical properties. However, since the FMs considered in this work are non-Gaussian, we introduce two additional statistics: the skewness and the Shannon entropy.

The skewness measures the asymmetry of the distribution around its mean and vanishes for a Gaussian distribution. We compute the skewness at a given pixel as

$$\text{Skew}[P_{ijk}^M] = \frac{1}{\sqrt{R}} \frac{\sum_{r=1}^R (P_{ijk}^{Mr} - \mu[P_{ijk}^M])^3}{\left(\sum_{r=1}^R (P_{ijk}^{Mr} - \mu[P_{ijk}^M])^2\right)^{3/2}}. \quad (9)$$

The final quantity used to characterize the FMs is the Shannon entropy [66]. Unlike moment-based statistics, the Shannon entropy probes the effective support of the probability distribution and provides a measure of how predictable the polarization amplitude is across realizations. In this work, we estimate the Shannon entropy using a simple binning approximation. For a fixed channel and pixel, the values of P_{ijk}^{Mr} across the R realizations are binned to obtain an empirical probability distribution $p_{ijk}^M(b)$. Here, b represents the index of the histogram bins used to discretize the polarization amplitude values across realizations. Note that the binning scheme is the same for all the pixels. We adopt $R = 1000$ realizations and $N_{\text{bins}} = 100$ bins. The Shannon entropy is then defined as

$$S[P_{ijk}^M] = - \sum_{b=1}^{N_{\text{bins}}} p_{ijk}^M(b) \ln p_{ijk}^M(b). \quad (10)$$

This computation is a first-order approximation because it neglects correlations between frequency channels

and between neighboring pixels. Nevertheless, for a fixed channel and pixel, it provides a useful indicator of the foreground signal's variability across realizations. This is particularly informative in template-based simulations, where large fractions of the sky exhibit vanishing or weak foreground emission and are therefore easier to predict than regions with large foreground amplitudes. An additional useful property of the Shannon entropy is that it is bounded from above by the value corresponding to a uniform distribution. For $N_{\text{bins}} = 100$, this maximum value is $\ln(100) \approx 4.6$.

B. Analysis of foreground models

The statistics described in the previous section are shown in Fig. 2 for the three FMs used to train the CNNs in this work. Since the pixel indices j and k are not fixed, each pixel in the analyzed block contributes a single value to the statistics. The resulting pixel-level values are therefore displayed as histograms.

The Shannon entropy distributions for the d11s6 and GP models show a significant fraction of pixels falling into bins consistent with $S \approx 0$. This behavior indicates that, for these models, certain pixels are highly predictable across realizations. In contrast, the entropy distribution of the RP model exhibits a nonzero lower bound, implying that no individual pixel is trivially predictable in this case. The skewness distributions further show that RP has the strongest asymmetry with respect to the mean. Finally, in terms of the variance, d11s6 and GP show less variability than the RP model. The mean values of all the metrics are summarized in Table II.

We define the statistical complexity of a foreground model as the degree of pixel-level variability, asymmetry, and unpredictability across realizations, as quantified by the variance, skewness, and Shannon entropy, respectively. According to these criteria, RP is identified as the most statistically complex FM, while d11s6 and GP exhibit a similar statistical behavior.

P (220 GHz)	GP	d11s6	RP
Variance [μK^2]	1.9	6.5	12.7
Skewness	4×10^{-3}	0.3	2.5
Shannon entropy	0.5	0.8	1.2

TABLE II. Mean values of the statistical metrics considered in this work (shown as vertical dotted lines in Fig. 2).

Based on these results, we formulate the following generalization hypothesis: CNNs trained on the RP model are expected to exhibit an improved performance if we test on FMs different from those used during training, compared to CNNs trained on d11s6 or GP. This generalization performance is computed with the performance metrics discussed in the following section.

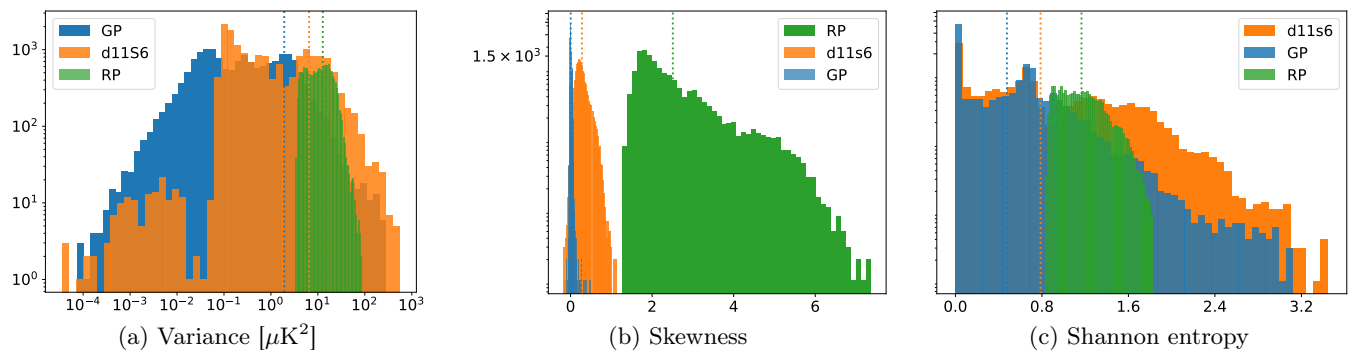


FIG. 2. Pixel-level distributions of the statistical metrics computed for the polarization amplitude $P = \sqrt{Q^2 + U^2}$ of the foreground models used for the training. The vertical dotted lines indicate the mean value over all pixels in the analyzed block, which are reported in Table II.

C. Performance metrics

In the previous section, we characterized the statistical properties of the FMs by computing the variance, skewness, and Shannon entropy, and used these quantities to establish a hierarchy of complexity among them. We now introduce a set of performance metrics designed to quantify the generalization capability of the CNN-based foreground-removal method. Our goal is to assess how accurately and precisely the reconstructed CMB maps reproduce the true CMB statistics when the foreground distribution differs from that seen during training. To this end, we compare the angular power spectra of the reconstructed and true CMB maps through the following dimensionless ratio, evaluated during the testing stage:

$$\text{rat}_\ell^{X,r}[M_1, M_2] = \frac{C_\ell^{\text{Rec},X,r}[M_1, M_2]}{C_\ell^{\text{True},X,r}[M_2]}, \quad (11)$$

where X denotes either E - or B -mode polarization, r labels realizations in the testing set, and the notation $[M_1, M_2]$ indicates that the CNN was trained on the FM M_1 and tested on FM M_2 . The set of FMs considered for training is $M_k \in \{\text{GP}, \text{d11s6}, \text{RP}\}$.

The numerator, $C_\ell^{\text{Rec},X,r}[M_1, M_2]$, is computed from the CNN-reconstructed map and, therefore, depends on both the training and testing models. The denominator, $C_\ell^{\text{True},X,r}[M_2]$, is obtained from the true CMB map associated with model M_2 and varies with the realization r . In the ideal case of perfect reconstruction, we expect $\text{rat}_\ell^{X,r}[M_1, M_2]$ to be consistent with 1, for all ℓ s. To quantify deviations from this ideal behavior, we compute summary statistics of the $\text{rat}_\ell^{X,r}$ distribution over realizations. As a robust estimator of central tendency, we compute the median

$$\text{Med}_\ell^X[M_1, M_2] = \text{median} \left[\text{rat}_\ell^{X,r}[M_1, M_2] \right]_r, \quad (12)$$

which provides a measure of the method's accuracy at each multipole. To characterize the spread of the distribution, we compute the 17th and 83rd percentiles, $p_\ell^{17,X}[M_1, M_2]$,

$p_\ell^{83,X}[M_1, M_2]$, respectively, and with them we define the uncertainty of the method as

$$\Delta_\ell^X[M_1, M_2] = \frac{p_\ell^{17,X}[M_1, M_2] + p_\ell^{83,X}[M_1, M_2]}{2}, \quad (13)$$

which corresponds to a central 68% probability interval. We employ medians and percentiles rather than means and standard deviations because the distribution of $\text{rat}_\ell^{X,r}$ is generally non-Gaussian and asymmetric. The quantity Δ_ℓ^X therefore provides a measure of the reconstruction's precision, quantifying the realization-to-realization scatter. If the method is unbiased, the median satisfies $\text{Med}_\ell^X[M_1, M_2] \approx 1$. Deviations from unity indicate a systematic offset in the reconstructed power spectrum. We therefore define the following estimator:

$$\text{bias}_\ell^X[M_1, M_2] = \left| \text{Med}_\ell^X[M_1, M_2] - 1 \right|, \quad (14)$$

which quantifies the accuracy of the cleaning method at each multipole. Small values of bias_ℓ^X indicate that the reconstructed spectrum is consistent with the true one, while larger values show systematic deviations.

We also compute the number of sigmas that the median deviates from 1 as a function of ℓ , combining both previous metrics as

$$N\sigma_\ell^X[M_1, M_2] = \left| \frac{\text{Med}_\ell^X[M_1, M_2] - 1}{\Delta_\ell^X[M_1, M_2]} \right|. \quad (15)$$

These metrics can be straightforwardly applied to other component-separation techniques, such as ILC or parametric methods, by replacing the CNN reconstruction with the corresponding traditional method. While the quantities defined above characterize the performance of a single CNN, we now introduce a metric that directly compares the generalization performance of two networks trained on different FMs. Specifically, we compare CNNs trained on models M_1 and M_2 when both are tested on a third model M_3 . We define the bias Generalization

Factor (bias-GF) as the difference between the averaged bias estimators,

$$\mathcal{G}\text{bias}_{[M_1, M_2; M_3]}^X = \left\langle \text{bias}_\ell^X[M_1, M_3] \right\rangle - \left\langle \text{bias}_\ell^X[M_2, M_3] \right\rangle, \quad (16)$$

where $\langle \cdot \rangle \equiv \langle \cdot \rangle_{\ell_{\min} < \ell < \ell_{\max}}$ denotes an average over the multipole range of interest. Analogously, we define a precision-based Generalization Factor (Δ -GF),

$$\mathcal{G}\Delta_{[M_1, M_2; M_3]}^X = \langle \Delta_\ell^X[M_1, M_3] \rangle - \langle \Delta_\ell^X[M_2, M_3] \rangle. \quad (17)$$

In our analysis we adopt $\ell_{\min} = 50$ and $\ell_{\max} = 260$. The notation $[M_1, M_2; M_3]$ indicates that the CNNs trained on M_1 and M_2 are compared under identical training conditions, differing only in the FM used to generate the training data, and are both evaluated on the same testing set generated with the FM M_3 . The sign of the Generalization Factor contains the relevant information: a negative value indicates that the CNN trained on M_1 yields smaller deviations from the true CMB spectrum than the one trained on M_2 when tested on M_3 . So, a negative value means that the CNN trained assuming M_1 generalizes better than the CNN trained assuming M_2 , when we test on M_3 . A positive value indicates the opposite. Due to the anti-symmetric property ($\mathcal{G}_{[M_1, M_2; M_3]}^X = -\mathcal{G}_{[M_2, M_1; M_3]}^X$) and the fact that $\mathcal{G}_{[M_k, M_k; M_3]}^X = 0$, only three independent comparisons exist when evaluating three foreground models. As discussed above, $\mathcal{G}\text{bias}$ quantifies averaged differences in accuracy, while $\mathcal{G}\Delta$ quantifies averaged differences in precision.

V. RESULTS

In this section, we present our results. We adopt the following color code: networks trained on GP are shown in blue, those trained on d11s6 in orange, and those trained on RP in green. Results from the parametric approach are shown in red, while those from the ILC are shown in purple. Throughout this section, we use a compact notation to describe the trained CNNs. We denote by Arch-Train a CNN with architecture "Arch" trained on a given FM "Train". For example, L3-GP corresponds to an L3-type network trained on the GP model.

A. Comparison with traditional methods

In Fig. 3, we present the results of foreground removal for the three FMs used to train the CNNs in this work, obtained with the parametric approach (red), the ILC (purple), and the CNN-based method, due to its specialized design for CMB applications, following the discussion in Section III C 3.

For the three FMs analyzed, we obtain better performance with the CNN-based method than with the traditional methods considered in this work. Moreover, we find that the traditional methods exhibit similar performance

across the three FMs used in this analysis. We must be careful when interpreting this result since, in this case, the CNNs were trained and tested on the same FM. This result, therefore, represents a consistency check, as such behavior is expected under these conditions. Since the goal of this paper is to assess the generalization capabilities of the CNN-based method, our main results are based on CNNs trained and tested on different FMs.

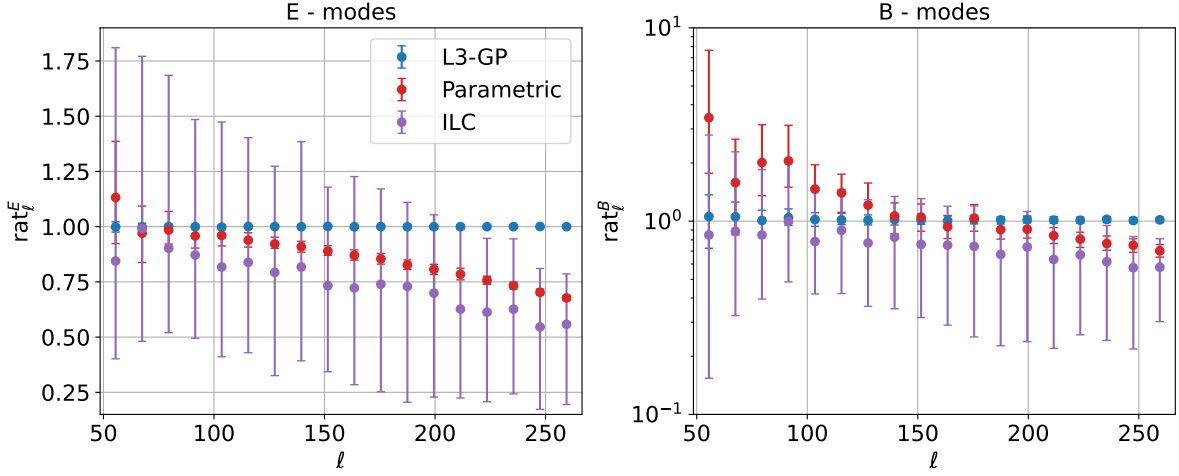
B. Qualitative generalization analysis

In Fig. 4, we show a qualitative comparison of the generalization capabilities of the CNN-based method using the L3 architecture. In each plot, we show the performance of two CNNs tested on the FM that was not used during training.

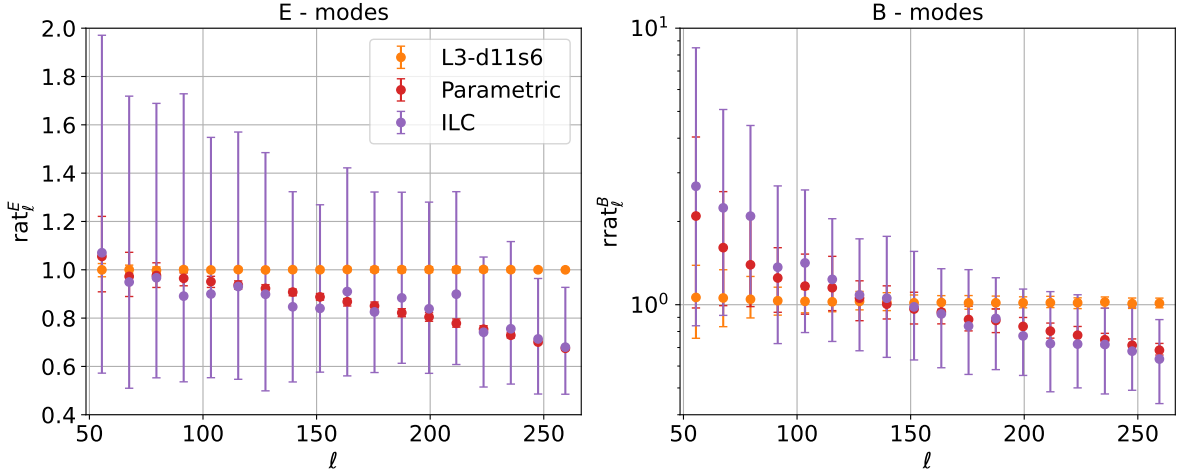
In Fig. 4.a, we show the results of L3-d11s6 and L3-RP tested on GP. For the E-modes, both CNNs show a similar median, but L3-RP has smaller error bars. For the B-modes, L3-RP has smaller error bars, and its median is also closer to 1. We therefore conclude that L3-RP performs better on GP than L3-d11s6. In Fig. 4.b, we show the results of L3-GP and L3-RP tested on d11s6. In this case, L3-RP shows better performance, both in terms of the size of the error bars and the median for the E- and B-modes. These two results agree with the prediction of the generalization hypothesis, which implies that training on the FM with higher statistical complexity improves the generalization capabilities of the CNNs. In Fig. 4.c, we show the performance of L3-GP and L3-d11s6 tested on RP. In this case, L3-GP shows better performance than L3-d11s6 for both the E- and B-modes. We interpret this result as a consequence of the fact that both GP and RP are directly related to the d1 template, while they differ slightly in the synchrotron model (s1 and s2). It is remarkable that the performance of L3-GP changes dramatically when tested on RP or d11s6. This suggests that the design of the training set is a key point for the CNN-based method, as the results of this CNN are highly sensitive to the FM used in the testing set.

In Fig. 5, we show the performance of the three CNNs on a fourth and a fifth model, d4s2 and d12s7, respectively, which were not used for the training of the CNNs.

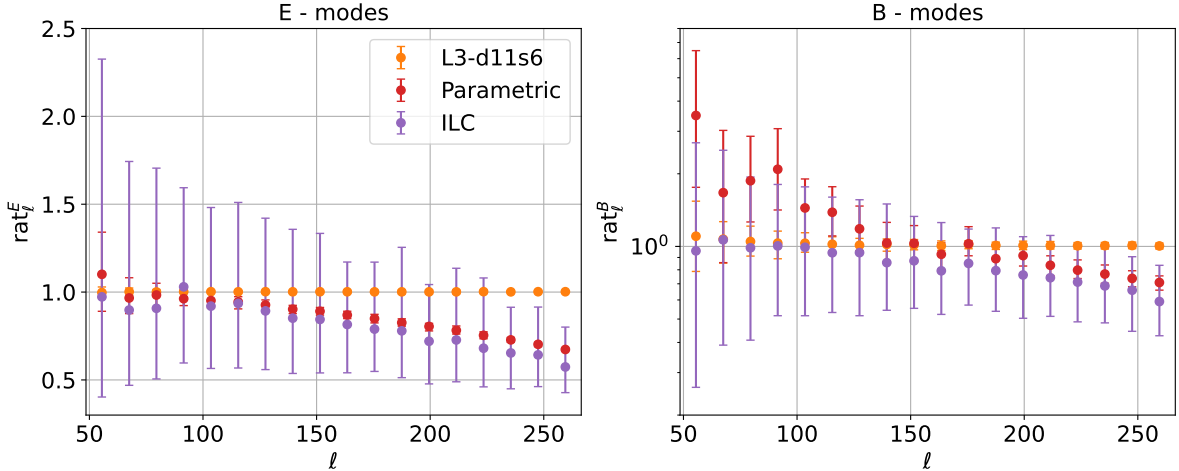
In Fig. 5.a, we show the results of the three trained L3 architectures on the fixed FM d4s2. In [34], it was found that L3-GP shows poor results when tested on d4s2. The authors then add d4s2 simulations to the training set, after which performance improves. In this work, we recover this result and show that L3-RP achieves improved performance without modifying the training set. In this case, we also find that L3-RP outperforms L3-d11s6, as predicted in Section IV B. In Fig. 5.b, we show the same CNNs tested on the model d12s7. The performance of L3-GP is the worst among the three, indicating a strong dependence of this CNN on the FM of the testing set. Furthermore, L3-RP performs better than L3-d11s6, supporting our prediction in Section IV B.



(a) Cleaning methods applied to the Gaussian Parameters (GP) foreground model. For the CNN-based method, we applied the L3 architecture trained on the GP model.



(b) Cleaning methods applied to the PySM3 d11s6 foreground model. For the CNN-based method, we applied the L3 architecture trained on the d11s6 model.



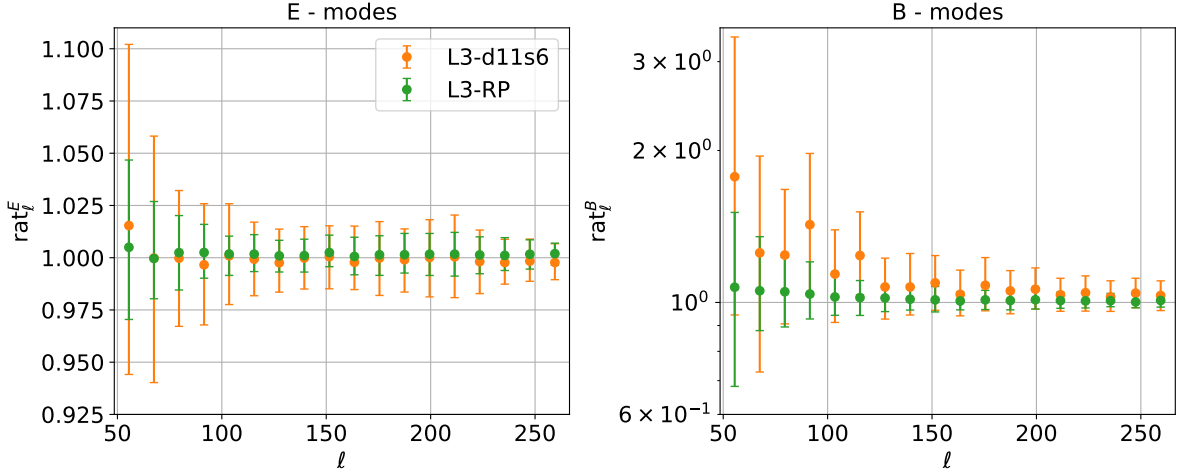
(c) Cleaning methods applied to the Rotating Patches (RP) foreground model. For the CNN-based method, we applied the L3 architecture trained on the RP model.

FIG. 3. Median and 68% Probability Interval (PI) of the ratio defined in Eq. 11. Left panels correspond to E-modes, while right panels correspond to B-modes. A logarithmic scale is used for the B-modes. We compare the CNN-based method with the traditional methods described in Sections III A and III B.

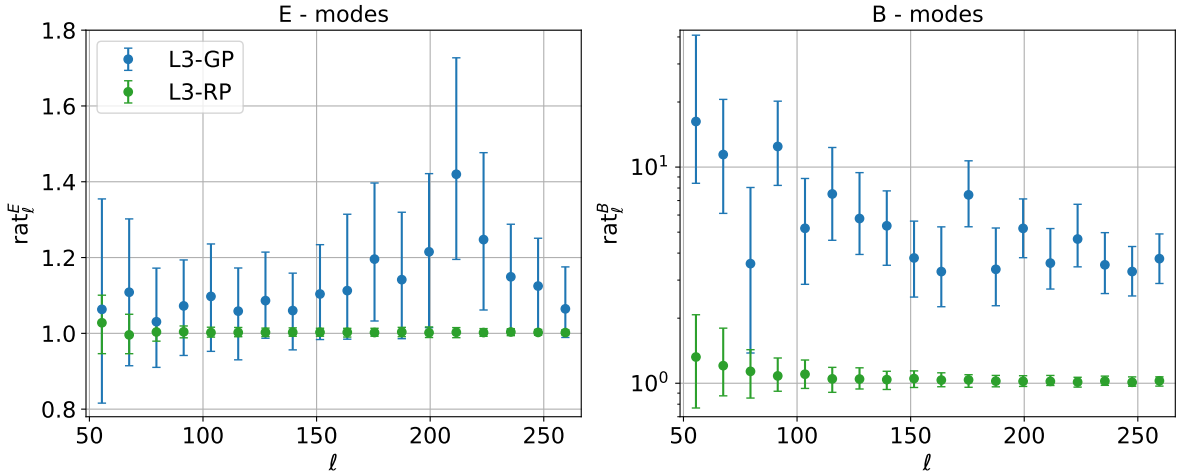
C. Quantitative generalization analysis

In Fig. 6, we show the averaged precision and accuracy metrics defined in Eqs. 13 and 14 for a fixed testing set.

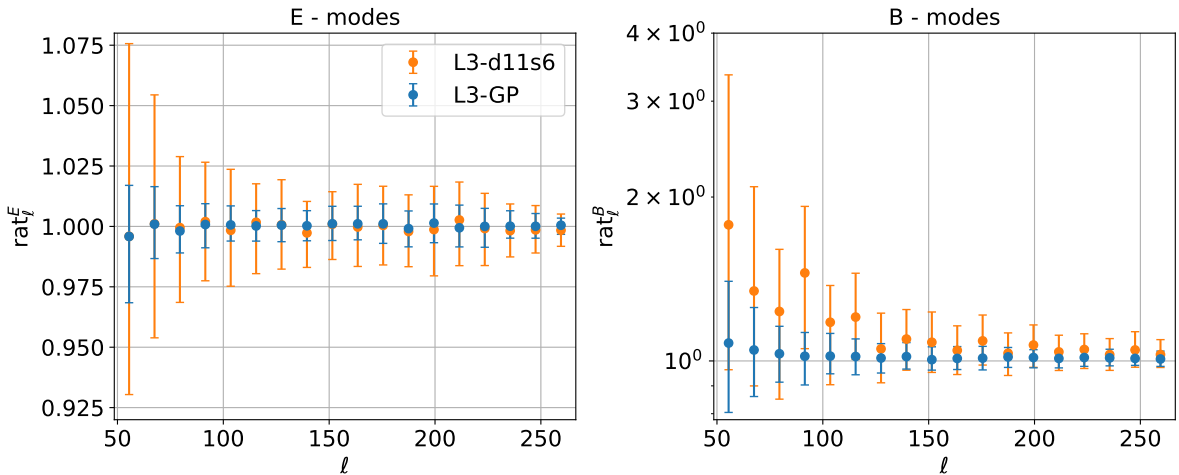
Fig. 6.a corresponds to the testing set generated with GP,



(a) Performance of the CNNs trained over the PySM3 model d11s6 and the Rotating Patches (RP) model and tested on the Gaussian Parameters (GP) model. L3-RP outperforms L3-d11s6 in both CMB E- and B-modes.



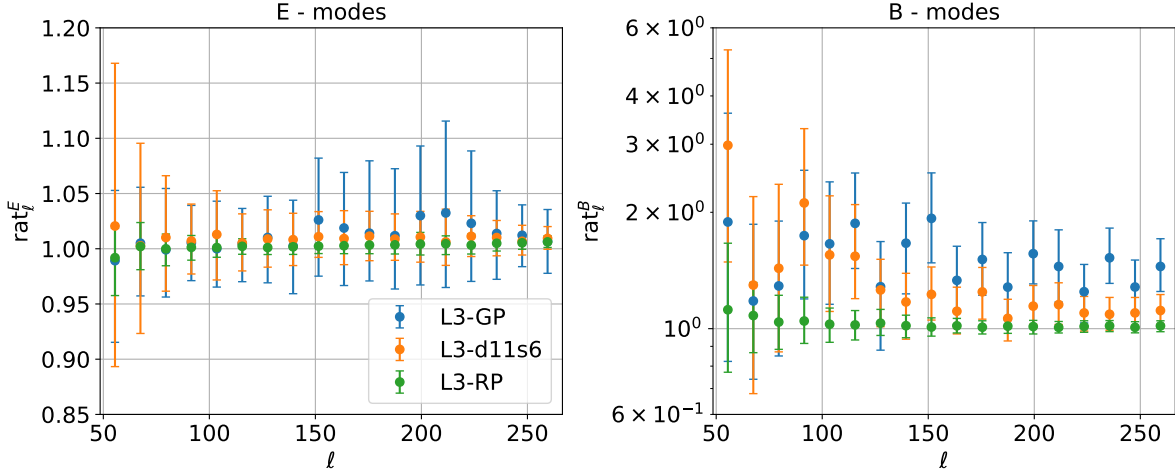
(b) Performance of the CNNs trained over the Rotating Patches (RP) model and the Gaussian Parameters (GP) and tested on the PySM3 model d11s6 model. L3-RP outperforms L3-GP in both CMB E- and B-modes.



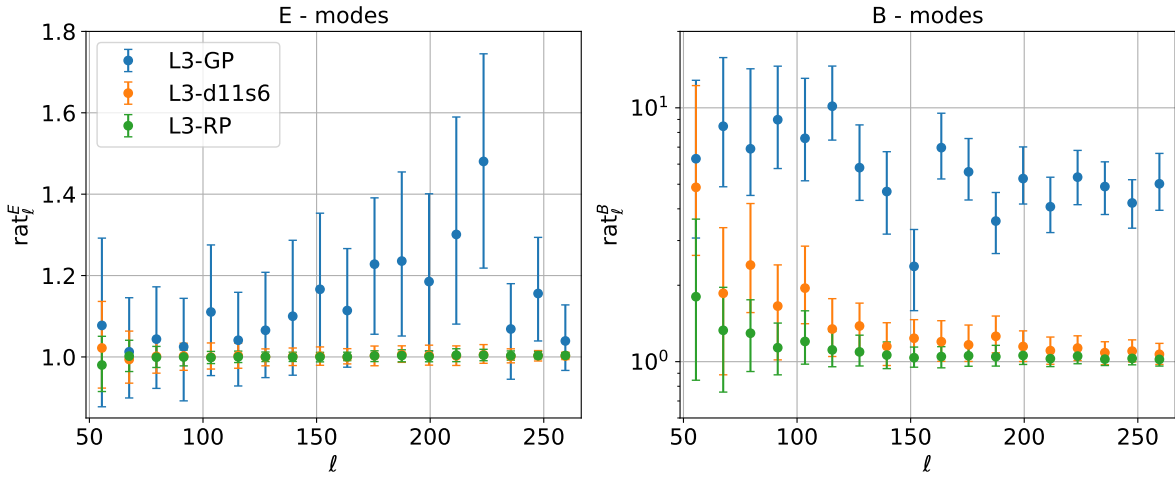
(c) Performance of the CNNs trained over the PySM3 model d11s6 and the Gaussian Parameters (GP) model and tested on the Rotating Patches (RP) model. L3-GP outperforms L3-d11s6 in both CMB E- and B-modes.

FIG. 4. Median and 68% Probability Interval (PI) of the ratio defined in Eq. 11. Left panels correspond to CMB E-modes, right panels to CMB B-modes. We compare two CNNs tested on a third foreground model.

Fig. 6.b to that generated with d11s6, and Fig. 6.c to that generated with RP. We compare different architectures



(a) Performance of the CNN-based method tested on the d4s2 model and trained on the 3 models shown in the legend.



(b) Performance of the CNN-based method tested on the d12s7 model and trained on the 3 models shown in the legend.

FIG. 5. Median and 68% Probability Interval (PI) of the ratio defined in Eq. 11. Left panels correspond to E-modes, right panels to B-modes. We compare the three CNNs with two fixed models that were not used during training.

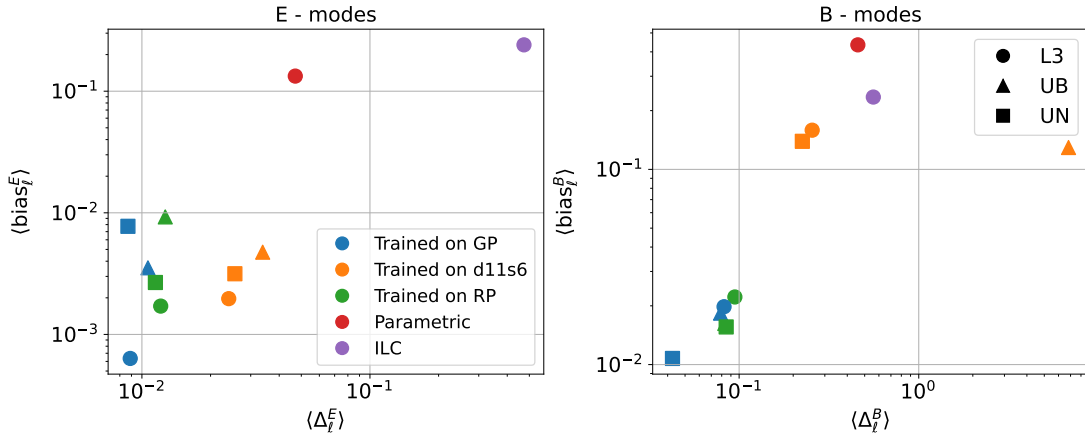
using markers and different colors to identify the FM used to train the CNN. We also include the traditional methods in the plots.

The x-axis of the plots in Fig. 6 corresponds to the averaged precision metric (the size of the error bars), while the y-axis to the averaged accuracy metric (the deviation from unity). The averaged metrics defined in this work allow us to quickly quantify the generalization capabilities. Both metrics are straightforward to interpret: the closer to the origin, the better. The results from Section VB can be recovered by looking at the circles and comparing green vs. orange (a), green vs. blue (b), and blue vs. orange (c). By looking at Figs. 6.a and 6.b, we conclude that the qualitative predictions made for the generalization capabilities hold for the UN and L3 architectures. For the UB architecture, UB-RP outperforms UB-d11s6 when we test on GP, supporting our prediction. However, UB-GP and UB-RP exhibit a similar performance to each other in three of the four averaged GFs. We leave understanding

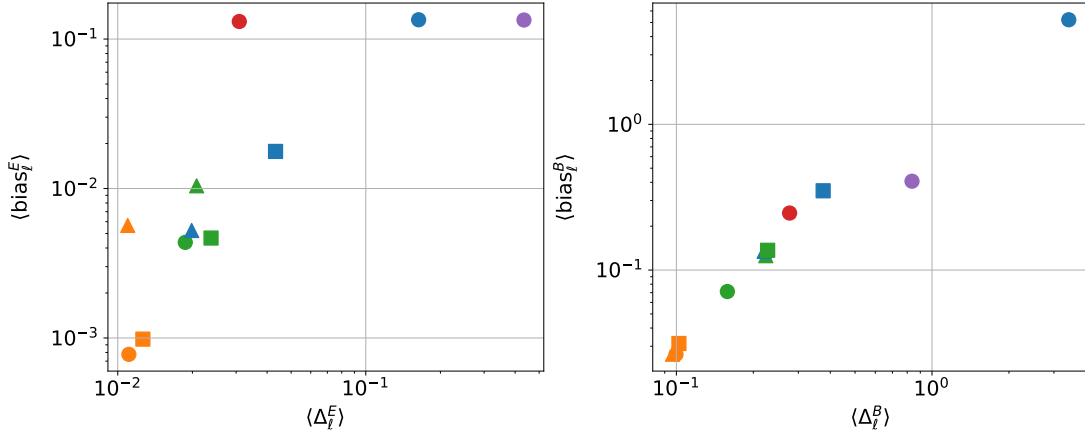
the relationship between batch normalization and the generalization capabilities to future work.

In Table III, we show the results for the generalization factors defined in Eqs. 17 and 16 for the three different architectures used in this work.

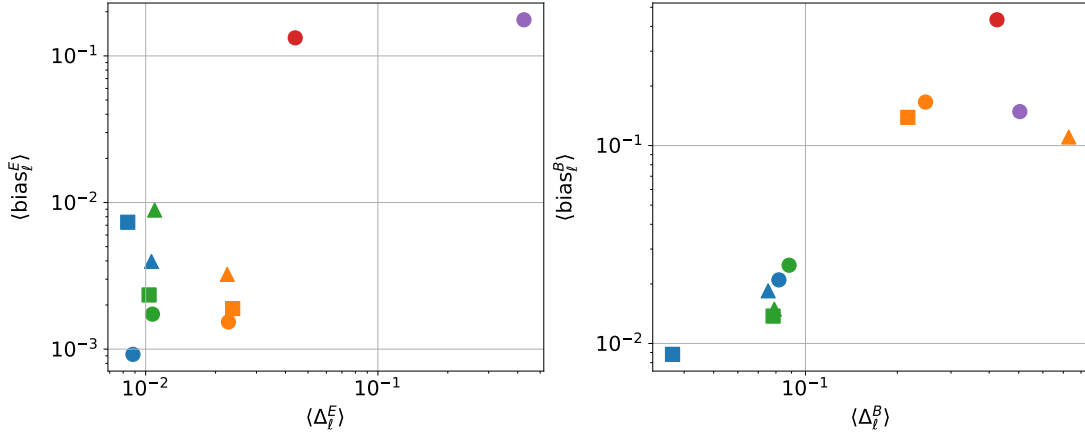
Table III summarizes the information contained in Fig. 6. Notably, the results for the UN and L3 architectures are similar, which implies that both architectures reach the same capabilities for foreground removal. By analyzing the sign of the GFs, we conclude that, for these two architectures, the CNNs trained with RP have better performance than the CNNs trained with d11s6 when tested on GP. The only performance metric that shows similar behavior, through a small value, corresponds to $\mathcal{G}_{\text{bias}}^E$, which can be confirmed for the L3 architecture, looking at Fig. 4.a. The CNNs trained with RP also outperform the CNNs trained with GP when tested on d11s6. The UB architecture shows similar behavior to the others, but with more GFs closer to zero when testing on d11s6.



(a) Performance metrics of the methods applied on the Gaussian Parameters (GP) model.



(b) Performance metrics of the methods applied on the PySM3 d11s6 model.



(c) Performance metrics of the methods applied on the Rotating Patches (RP) model.

FIG. 6. Accuracy and precision metrics (Eqs. 13 and 14) averaged over the multipole range of interest ($50 < \ell < 260$). Left panels correspond to CMB E-modes, right panels to CMB B-modes. Each architecture is represented by a different marker, and the foreground model used to generate the training set is represented by a different color.

Except for this case, we reach the same conclusions as before. On the other hand, when we compare UB and UN, the performance metrics do not show a clear pattern in which UB outperforms UN. This suggests, at least for the case studied in this work, that better control of

the gradients during training does not necessarily generate an improved performance of the CNN-based method. Finally, all the CNNs trained with GP outperform the CNNs trained with d11s6 when tested on RP. As discussed before, we attribute this to the fact that RP and GP are

		[d11s6, RP; GP]	[RP, GP; d11s6]	[GP, d11s6; RP]
L3	$\mathcal{G}\text{bias}^E$	3×10^{-4}	-0.1	6×10^{-4}
	$\mathcal{G}\Delta^E$	0.01	-0.1	-0.01
	$\mathcal{G}\text{bias}^B$	0.1	-5	-0.2
	$\mathcal{G}\Delta^B$	0.2	-3	-0.2
UN	$\mathcal{G}\text{bias}^E$	5×10^{-4}	-0.01	5×10^{-4}
	$\mathcal{G}\Delta^E$	0.02	-0.02	-0.01
	$\mathcal{G}\text{bias}^B$	0.1	-0.2	-0.1
	$\mathcal{G}\Delta^B$	0.1	-0.2	-0.2
UB	$\mathcal{G}\text{bias}^E$	-4×10^{-3}	5×10^{-3}	10^{-3}
	$\mathcal{G}\Delta^E$	0.02	10^{-3}	-0.01
	$\mathcal{G}\text{bias}^B$	0.1	-0.01	-0.09
	$\mathcal{G}\Delta^B$	7	3×10^{-3}	-0.7

TABLE III. Generalization Factor (GF) for the relevant combinations. If a given GF $[M_1, M_2; M_3]$ shows a negative value, it means that the CNN trained on M_1 outperforms, and so generalizes better, than the CNN trained on M_2 , testing on M_3 . A positive value means the opposite.

two models based on the same d1 template for the dust.

In Fig. 7, we show the number of standard deviations that the median ratio deviates from unity for the L3 architecture when tested on FMs not used during training. This metric provides a stringent test of the method’s reliability; a value greater than one indicates that the 68% probability interval does not encompass the true CMB power spectrum. We find that the largest systematic deviations occur for L3-GP when tested on d11s6, representing the only case where the E-mode bias exceeds 1σ . For B-modes, L3-GP on d11s6 remains the poorest performer, though both L3-d11s6 tested on GP and L3-d11s6 tested on RP reach $N\sigma \approx 1$ at $\ell \approx 100$. Such deviations are particularly problematic for experiments targeting the recombination bump at low multipoles, where accuracy is paramount. In contrast, the CNNs trained on the RP model demonstrate the highest consistency across unseen test sets, maintaining $N\sigma$ values well below unity across the entire multipole range.

VI. CONCLUSION

In this work, we studied the generalization capabilities of a CNN-based method for Galactic foreground removal in CMB polarization maps. We show that training the

CNNs assuming the statistically simplest model can introduce systematic errors in the method, whereas training assuming the statistically most complex model improves foreground removal performance. The introduced foreground model (FM) statistics allow us to interpret the generalization results obtained with the CNN-based method. In particular, the variance, skewness, and Shannon entropy of the FMs indicate that the Rotating Patches (RP) foreground model is the most statistically complex model among the three considered in this work. We consistently show that CNNs trained on RP achieve better performance when tested on FMs not used during training. This result supports our generalization hypothesis: training on more statistically complex FMs leads to improved generalization across different scenarios.

Beyond the FM statistics, we introduce quantitative performance metrics to assess generalization capabilities that are often discussed only qualitatively. We show that the interpretation of generalization in terms of these metrics is consistent with the qualitative analysis and provides a new framework for studying generalization in a fully quantitative manner. These metrics further indicate that the L3 and UN architectures exhibit similar generalization capabilities, which is not a trivial result given their architectural differences.

Although CNN-based methods generally outperform the traditional foreground-cleaning techniques studied in this work, their results cannot be considered reliable without a proper understanding of their generalization properties. In particular, an insufficient understanding of generalization limits our ability to define robust and meaningful error bars. A clear example of this limitation is provided by the L3 CNN trained on the Gaussian Parameters (GP) model, which yields the worst performance when tested on the PySM3 d11s6, d4s2 and d12s7 models, while producing one of the best results when tested on RP. This behavior highlights the risks of drawing conclusions from CNN-based methods without a careful assessment of their range of generalization.

VII. ACKNOWLEDGEMENTS

This work was supported by the National Science Foundation under Cooperative Agreement PHY-2019786 (The NSF AI Institute for Artificial Intelligence and Fundamental Interactions, <http://iaifi.org/>).

[1] A. H. Guth, *Physical Review D* **23**, 347 (1981).
[2] A. Linde, *Physics Letters B* **108**, 389 (1982).
[3] P. A. Ade, Z. Ahmed, M. Amiri, D. Barkats, R. B. Thakur, C. Bischoff, D. Beck, J. Bock, H. Boenish, E. Bullock, et al., *Physical review letters* **127**, 151301 (2021).

[4] M. Tristram, A. J. Banday, K. M. Gorski, R. Kesitalo, C. R. Lawrence, K. J. Andersen, R. B. Barreiro, J. Borrill, L. P. L. Colombo, H. K. Eriksen, R. Fernandez-Cobos, T. S. Kisner, E. Martinez-Gonzalez, B. Partridge, D. Scott, T. L. Svalheim, and I. K. Wehus, *Physical Review D* **105**, 083524 (2022).

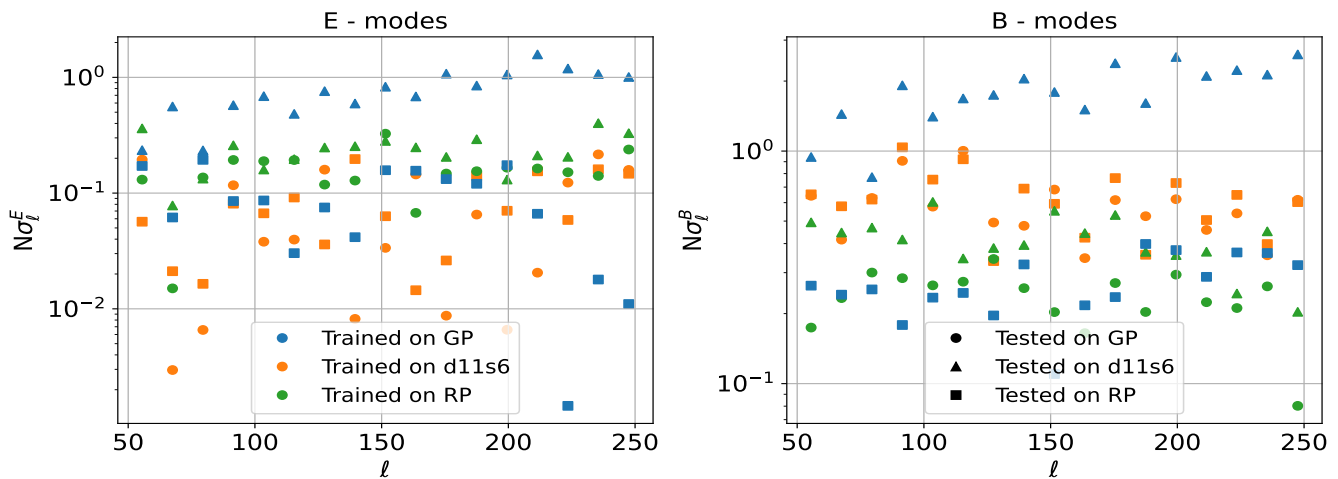


FIG. 7. Deviations from a median equal to one computed following Eq. 15. Here, we consider the L3 architecture. The color specifies the model assumed during training, while the marker refers to the model used for testing. We do not show CNNs trained and tested on the same foreground model.

- [5] M. Tegmark and G. Efstathiou, *Monthly Notices of the Royal Astronomical Society* **281**, 1297 (1996).
- [6] W. Hu, M. M. Hedman, and M. Zaldarriaga, *Physical Review D* **67**, 043004 (2003).
- [7] S. Stellati, F. Piacentini, S. Micheli, A. Novelli, F. Columbro, A. Coppolecchia, P. de Bernardis, S. Masi, M. Najafi, A. Occhiuzzi, *et al.*, arXiv preprint arXiv:2509.03564 (2025).
- [8] A. Lewis and A. Challinor, *Physics Reports* **429**, 1 (2006).
- [9] S. Belkner, J. Carron, L. Legrand, C. Umiltà, C. Pryke, C. Bischoff, C.-S. Collaboration, *et al.*, *The Astrophysical Journal* **964**, 148 (2024).
- [10] P. A. Ade, N. Aghanim, Z. Ahmed, R. W. Aikin, K. D. Alexander, M. Arnaud, J. Aumont, C. Baccigalupi, A. J. Banday, D. Barkats, *et al.*, *Physical review letters* **114**, 101301 (2015).
- [11] Y. Akrami, M. Ashdown, J. Aumont, C. Baccigalupi, M. Ballardini, A. J. Banday, R. Barreiro, N. Bartolo, S. Basak, K. Benabed, *et al.*, *Astronomy & Astrophysics* **641**, A11 (2020).
- [12] F. A. Martire, R. B. Barreiro, and E. Martínez-González, *Journal of Cosmology and Astroparticle Physics* **2022** (04), 003.
- [13] S. K. Choi and L. A. Page, *Journal of Cosmology and Astroparticle Physics* **2015** (12), 020.
- [14] F. Bianchini, D. Beck, W. K. Wu, Z. Ahmed, S. Belkner, J. Carron, B. S. Hensley, C. L. Pryke, C. Umiltà, and C.-S. Collaboration, *The Astrophysical Journal* **993**, 105 (2025).
- [15] R. Stompor, S. Leach, F. Stivoli, and C. Baccigalupi, *Monthly Notices of the Royal Astronomical Society* **392**, 216 (2009).
- [16] D. Poletti and J. Errard, *Astrophysics Source Code Library*, ascl (2023).
- [17] K. Abazajian, G. E. Addison, P. Adshead, Z. Ahmed, D. Akerib, A. Ali, S. W. Allen, D. Alonso, M. Alvarez, M. A. Amin, *et al.*, *The Astrophysical Journal* **926**, 54 (2022).
- [18] C. Bennett, G. Smoot, G. Hinshaw, E. Wright, A. Kogut, G. De Amici, S. Meyer, R. Weiss, D. Wilkinson, S. Gulkis, *et al.*, *Astrophysical Journal, Part 2-Letters (ISSN 0004-637X)*, vol. 396, no. 1, Sept. 1, 1992, p. L7-L12. Research supported by NASA. **396**, L7 (1992).
- [19] C. L. Bennett, R. S. Hill, G. Hinshaw, M. Nolta, N. Odegard, L. Page, D. Spergel, J. Weiland, E. Wright, M. Halpern, *et al.*, *The Astrophysical Journal Supplement Series* **148**, 97 (2003).
- [20] M. Tegmark, A. de Oliveira-Costa, and A. J. Hamilton, *Physical Review D* **68**, 123523 (2003).
- [21] H. K. Eriksen, A. Banday, K. Górski, and P. Lilje, *The Astrophysical Journal* **612**, 633 (2004).
- [22] J. Delabrouille, J.-F. Cardoso, M. Le Jeune, M. Betoule, G. Fay, and F. Guillaux, *Astronomy & Astrophysics* **493**, 835 (2009).
- [23] M. Remazeilles, J. Delabrouille, and J.-F. Cardoso, *Monthly Notices of the Royal Astronomical Society* **410**, 2481 (2011).
- [24] C. Leloup, J. Errard, and R. Stompor, *Physical Review D* **108**, 123547 (2023).
- [25] L. Gomez Bachar, A. T. Chantada, S. J. Landau, C. G. Scoccola, and P. Protopapas, *Physical Review D* **112**, 10.1103/8mpc-8wmc (2025).
- [26] S. Kannan, T. Qiu, C. Cuesta-Lazaro, and H. Jeong, arXiv preprint arXiv:2507.11842 (2025).
- [27] J. Zeghal, D. Lanzieri, F. Lanusse, A. Boucaud, G. Louppe, E. Aubourg, and A. E. Bayer, *Astronomy & Astrophysics* **699**, A327 (2025).
- [28] S.-F. Chen, K.-F. Chen, and C. Dvorkin, *Journal of Cosmology and Astroparticle Physics* **2025** (11), 082.
- [29] A. Akhmetzhanova, S. Mishra-Sharma, and C. Dvorkin, *Monthly Notices of the Royal Astronomical Society* **527**, 7459 (2024).
- [30] G. Zhang, A. C. Sengul, and C. Dvorkin, *Monthly Notices of the Royal Astronomical Society* **527**, 4183 (2023), <https://academic.oup.com/mnras/article-pdf/527/2/4183/53788979/stad3521.pdf>.

- [31] J. Casas, L. Bonavera, J. González-Nuevo, C. Baccigalupi, M. Cueli, D. Crespo, E. Goitia, J. Santos, M. Sánchez, and F. de Cos, *Astronomy & Astrophysics* **666**, A89 (2022).
- [32] G.-J. Wang, H.-L. Shi, Y.-P. Yan, J.-Q. Xia, Y.-Y. Zhao, S.-Y. Li, and J.-F. Li, *The Astrophysical Journal Supplement Series* **260**, 13 (2022).
- [33] Y.-P. Yan, G.-J. Wang, S.-Y. Li, and J.-Q. Xia, *The Astrophysical Journal* **947**, 29 (2023).
- [34] Y.-P. Yan, S.-Y. Li, G.-J. Wang, Z. Zhang, and J.-Q. Xia, *The Astrophysical Journal Supplement Series* **274**, 4 (2024).
- [35] D. Heurtel-Depeiges, B. Burkhart, R. Ohana, and B. R.-S. Blancard, arXiv preprint arXiv:2310.16285 (2023).
- [36] F. McCarthy, J. C. Hill, W. R. Coulton, and D. W. Hogg, *Physical Review D* **111**, 063549 (2025).
- [37] S. K. Yadav, [A perceptron based ilc method to obtain accurate cmb b-mode angular power spectrum](#) (2024), arXiv:2411.01233 [astro-ph.CO].
- [38] A. J. Duivenvoorden, K. Surrao, A. E. Bayer, A. E. Adler, N. Dachlythra, S. Azzoni, and J. C. Hill, arXiv preprint arXiv:2512.16869 (2025).
- [39] M. H. Abitbol, Z. Ahmed, D. Barron, R. B. Thakur, A. N. Bender, B. A. Benson, C. A. Bischoff, S. A. Bryan, J. E. Carlstrom, C. L. Chang, *et al.*, arXiv preprint arXiv:1706.02464 (2017).
- [40] K. N. Abazajian, P. Adshead, Z. Ahmed, S. W. Allen, D. Alonso, K. S. Arnold, C. Baccigalupi, J. G. Bartlett, N. Battaglia, B. A. Benson, *et al.*, arXiv preprint arXiv:1610.02743 (2016).
- [41] K. M. Górski, E. Hivon, A. J. Banday, B. D. Wandelt, F. K. Hansen, M. Reinecke, and M. Bartelmann, *ApJ* **622**, 759 (2005), arXiv:astro-ph/0409513.
- [42] A. Zonca, L. Singer, D. Lenz, M. Reinecke, C. Rosset, E. Hivon, and K. Gorski, *Journal of Open Source Software* **4**, 1298 (2019).
- [43] J.-C. Hamilton, L. Mousset, E. Battistelli, P. De Bernardis, M.-A. Bigot-Sazy, P. Chaniai, R. Charlassier, G. D'Alessandro, M. De Petris, M. G. Lerena, *et al.*, *Journal of Cosmology and Astroparticle Physics* **2022** (04), 034.
- [44] L. Mousset, M. G. Lerena, E. Battistelli, P. De Bernardis, P. Chaniai, G. d'Alessandro, G. Dashyan, M. De Petris, L. Grandsire, J.-C. Hamilton, *et al.*, *Journal of Cosmology and Astroparticle Physics* **2022** (04), 035.
- [45] S. Torchinsky, J.-C. Hamilton, M. Piat, E. Battistelli, P. De Bernardis, C. Chapron, G. d'Alessandro, M. De Petris, M. G. Lerena, M. González, *et al.*, *Journal of Cosmology and Astroparticle Physics* **2022** (04), 036.
- [46] A. Lewis, A. Challinor, and A. Lasenby, *The Astrophysical Journal* **538**, 473 (2000).
- [47] N. Aghanim *et al.*, *Astron. Astrophys* **641**, A6 (2020).
- [48] M. Reinecke, S. Belkner, and J. Carron, *Astronomy & Astrophysics* **678**, A165 (2023).
- [49] D. Alonso, J. Sanchez, A. Slosar, and L. D. E. S. Collaboration, *Monthly Notices of the Royal Astronomical Society* **484**, 4127 (2019).
- [50] J. Grain, M. Tristram, and R. Stompor, *Physical Review D-Particles, Fields, Gravitation, and Cosmology* **79**, 123515 (2009).
- [51] N. Galitzki, T. Tsan, J. Spisak, M. Randall, M. Silva-Feaver, J. Seibert, J. Lashner, S. Adachi, S. M. Adkins, T. Alford, *et al.*, *The Astrophysical Journal Supplement Series* **274**, 33 (2024).
- [52] K. W. Yoon, P. A. Ade, D. Barkats, J. Battle, E. Bierman, J. Bock, J. Brevik, H. Chiang, A. Crites, C. Dowell, *et al.*, in *Millimeter and Submillimeter Detectors and Instrumentation for Astronomy VIII* (SPIE, 2006) pp. 508–525.
- [53] A. Schillaci, P. Ade, Z. Ahmed, M. Amiri, D. Barkats, R. B. Thakur, C. Bischoff, J. Bock, H. Boenish, E. Bullock, *et al.*, *Journal of Low Temperature Physics* **199**, 976 (2020).
- [54] A. Zonca, B. Thorne, N. Krachmalnicoff, and J. Borrill, *Journal of Open Source Software* **6**, 3783 (2021).
- [55] R. e. a. Adam, *Astronomy & Astrophysics* **594**, A10 (2016).
- [56] C. L. Bennett, D. Larson, J. L. Weiland, N. Jarosik, G. Hinshaw, N. Odegard, K. Smith, R. Hill, B. Gold, M. Halpern, *et al.*, *The Astrophysical Journal Supplement Series* **208**, 20 (2013).
- [57] D. P. Finkbeiner, M. Davis, and D. J. Schlegel, *The Astrophysical Journal* **524**, 867 (1999).
- [58] G. Martínez-Solaesche, A. Karakci, and J. Delabrouille, *MNRAS* **476**, 1310 (2018), arXiv:1706.04162 [astro-ph.CO].
- [59] A. Kogut, *The Astrophysical Journal* **753**, 110 (2012).
- [60] R. Fernandez-Cobos, A. Marcos-Caballero, P. Vielva, E. Martínez-González, and R. B. Barreiro, *Monthly Notices of the Royal Astronomical Society* **459**, 441 (2016).
- [61] Z. Zhang, Y. Liu, S.-Y. Li, D.-L. Wu, H. Li, and H. Li, *Journal of Cosmology and Astroparticle Physics* **2022** (07), 044.
- [62] J. Kim, P. Naselsky, and P. R. Christensen, *Physical Review D-Particles, Fields, Gravitation, and Cosmology* **79**, 023003 (2009).
- [63] S. Basak and J. Delabrouille, *Monthly Notices of the Royal Astronomical Society* **435**, 18 (2013).
- [64] O. Ronneberger, P. Fischer, and T. Brox, *U-net: Convolutional networks for biomedical image segmentation* (2015), arXiv:1505.04597 [cs.CV].
- [65] J. Bjorck, C. Gomes, B. Selman, and K. Q. Weinberger, *Understanding batch normalization* (2018), arXiv:1806.02375 [cs.LG].
- [66] C. E. Shannon, *The Bell system technical journal* **27**, 379 (1948).